PHYSICAL REVIEW B **97**, 094109 (2018)

Lattice dynamics, phase transition, and tunable fundamental band gap of photovoltaic (K,Ba)(Ni,Nb)$O_{3-\delta}$ ceramics from spectral measurements and first-principles calculations

Chuanqian Li (李传青),[1] Fang Wang (王芳),[1] Yuyun Sun (孙钰云),[1] Kai Jiang (姜凯),[1] Shijing Gong (龚士静),[1]
Zhigao Hu (胡志高),[1,2,*] Zhiyong Zhou (周志勇),[3] Xianlin Dong (董显林),[3] and Junhao Chu (褚君浩)[1]
[1]*Key Laboratory of Polar Materials and Devices (MOE) and Technical Center for Multifunctional Magneto-Optical Spectroscopy (Shanghai), Department of Electronic Engineering, East China Normal University, Shanghai 200241, China*
[2]*Collaborative Innovation Center of Extreme Optics, Shanxi University, Taiyuan, Shanxi 030006, China*
[3]*Key Laboratory of Inorganic Functional Materials and Devices, Shanghai Institute of Ceramics, Chinese Academy of Sciences, Shanghai 200050, China*

(Received 11 December 2017; revised manuscript received 1 March 2018; published 22 March 2018)

Ferroelectrics have long been recognized as one of the candidate class of materials for applications in photovoltaic devices. Recently, ferroelectric perovskite (K,Ba)(Ni,Nb)$O_{3-\delta}$ has been successfully synthesized and demonstrated to have a near-optimal band gap (1.39 eV), exhibiting good photovoltaic performance. However, the connection between the structural order-disorder transformation, electronic structure, bulk photovoltaic, and photocatalytic properties remains not well understood. Here, we investigate the phase transition evolutions of lead-free $[KNbO_3]_{1-x}[BaNi_{1/2}Nb_{1/2}O_{3-\delta}]_x$ (KBNNOx, $x = 0$–0.5) ceramics via x-ray diffraction (XRD), Raman scattering, and computational evidences. The lattice dynamics and the origin of the successive rhombohedral→orthorhombic→tetragonal→cubic phase transitions have been systemically explored based on temperature-dependent XRD peak positions and phonon modes under different geometries. Moreover, the differences in the phase transition temperature and interior structure between the solid solution $x = 0.2$ and the end member $x = 0$ highlight local and nonlocal characteristics, which are helpful for understanding the photovoltaic mechanisms. Additionally, the robust photocatalytic decoloration effect on methylene blue can further confirm the photon-generated carrier behavior in the partly structural disordered orthorhombic phase. This identification of structural phases, combined with the ability to perform photocatalytic decoloration, give some insights on promising oxide applications as semiconducting ferroelectric absorbers and carrier-separating layers in photocatalytic or photovoltaic devices.

DOI: 10.1103/PhysRevB.97.094109

I. INTRODUCTION

Grinberg first described the photovoltaic effect of $[KNbO_3]_{1-x}[BaNi_{1/2}Nb_{1/2}O_{3-\delta}]_x$ (KBNNOx) solid solutions in 2013, and the connection between the noncentrosymmetric materials' structure, electronic structure, and bulk photovoltaic performance was elaborated using a first-principles calculation two years later [1,2]. Recently, KBNNOx ferroelectrics (FEs) with an adjustable band gap range of $E_g = 1.1$–3.8 eV have gained even more attention because it is one of the prominent alternatives to conventional semiconductor junctions for photoexcited carrier separation and photovoltaic solar energy conversion [3–8], exhibiting ferroelectric polarization, domain walls/Shockley-Queisser limit-induced carrier separation mechanisms, and the bulk photovoltaic effect (BPVE) [9–12]. Interestingly, the intrinsic polarization of FEs promotes the separation of photoexcited carriers and inhibits radiative or nonradiative recombination with the holes, avoiding the need for a p-n junction or heterojunction to separate charge. Therefore, photovoltages as the most important characterization of the photoresponse in FEs can exceed several times their band-gap values, which indicates that the FEs are able of capturing a vast range of the solar spectrum and potentially enabling a higher solar energy conversion efficiency than the Shockley-Queisser limit. Accompanied with light absorption, electrons are excited from an O $2p$ valence to a transition-metal d conduction band for electricity or catalysis generation [13]. For example, a weakly ferroelectric nonperovskite $KBiFe_2O_5$ material has been discovered with the robust photocatalytic decoloration effect on methylene blue [14]. This finding may open an avenue to discovering and designing optimal FE compounds for solar energy applications.

As a typical ABO_3, $BiFeO_3$ has long been recognized to possess the narrowest band gap ($E_g \sim 2.7$ eV) among robust FE-based materials, while most conventional ferroelectric materials have band gaps wider than 2.7 eV, which limit their ability to absorb the visible light that makes up the largest fraction of the solar irradiance [15]. Therefore, improvements in photovoltaic efficiency have been inhibited against the wide band gaps of FEs. The inclusion of transition-metal cations at the B site in $PbTiO_3$ [16] has been proposed as a strategy to decrease the band gap [17–19]. Some other studies suggested that doping the TiO_6 network with an oxygen-vacancy-stabilized d^8 M^{2+} (M = Ni, Pd, Pt, and Ce) may decrease E_g to below 2.0 eV [16,20]. However, these hypothetical compounds have not been synthesized in experiments. Following the excellent properties (high Curie temperature, giant piezoelectricity,

---

[*] zghu@ee.ecnu.edu.cn

and large polarization) and band-gap-engineering strategy explored in a previous study on A-site (A = Na, Li, La)-doped $KNbO_3$ (KNNO and KLNO) and Ni-doped $PbTiO_3$ [21–26], the introduction of Ba^{2+}/Ni^{2+} onto A/B-site $KNbO_3$ in the solid solution $[KNbO_3]_{1-x}[BaNi_{1/2}Nb_{1/2}O_{3-\delta}]_x$ (abbreviated as KBNNOx) was shown to result in a significant decrease in the band gap without loss of ferroelectric ordering [1,2].

While this novel material has substantially advanced the area of ferroelectric photovoltaics, there remain open questions. For example, the doping effects on structure distortion and physical properties (i.e., catalysis and ferromagnetism) of KBNNOx ceramics have not been well investigated. Moreover, no study on a combination of temperature-dependent x-ray diffraction and Raman scattering has been reported on KBNNOx ceramics. Raman scattering and x-ray diffraction are nondestructive and attractive probe techniques, which can detect molecular vibration, lattice thermal expansion, and collect some invaluable information on nonuniform lattice distortion and structural variations. Furthermore, it is reported that temperature-dependent phonon modes are effective strategies to explore the origin of lattice instabilities. Especially, phonon frequencies as a function of temperature could be a crucial tool to investigate phase transformations. Note that the structural transitions can give an important insight on the ferroelectric, dielectric, and photovoltaic properties of ferroelectric oxides. Therefore, it is necessary to further investigate the phase transitions with the aid of Raman scattering under different conditions, such as compositions, temperature, cross (VH), parallel (VV), and nonpolarized.

In this paper, structural distortion with different BNNO compositions has been examined by temperature-dependent x-ray diffraction and Raman scattering. The optical phonon modes are classified mainly as lattice translations involving the motion of atoms or ions and the internal modes of NbO_6 octahedra. Moreover, the physical mechanisms of the separation from photoexcited carriers are explained with the aid of first-principles calculations and photocatalytic activity. Finally, based on the analysis of thermal evolutions and theoretical evidence, phase transformation diagrams can be well determined.

II. EXPERIMENTAL DETAILS

Ceramics of (1-x)$KNbO_3$-$x$$BaNi_{1/2}Nb_{1/2}O_{3-\delta}$ (KBNNOx, $x = 0.0$, 0.1, 0.2, 0.3, 0.4, and 0.5, abbreviated as KNO, KBNNO1, KBNNO2, KBNNO3, KBNNO4, and KBNNO5, respectively) are synthesized by standard solid state reaction methods followed by a sintering process. The precursor materials, including high-purity K_2CO_3 (99.5%), $BaCO_3$ (99.95%), NiO (98%, green or black), and Nb_2O_5 (99.99%) powder are dried at 373 K to remove the absorbed moisture. Stoichiometric quantities of dried precursor powders are mixed in a grinding bowl and ball milled for 24 h in ethanol. After the evaporation of ethanol, the precursor mixed powders are pressed into disks of 15 mm diameter and 2 mm in thickness and then calcined in a covered alumina crucible, surround by the 2 mol K_2CO_3 and 1 mol Nb_2O_5 mixtures for sacrificial powder in order to inhibit the volatilization of potassium. For KNO the disk is calcined at 873 K for 6 h and 1073 K for 6 h, while for the KBNNO1–KBNNO5 samples, 1173 K for 12 h is used. Then the calcined disks are ball milled for 24 h again, and approximately 1.2 g aliquots are pressed into pellets with a diameter of 10 mm and thickness of 2 mm at a pressure of 20 MPa in uniaxial pressing. To improve the sinterability, two additional measures are adopted. They are sintering at temperatures close to the melting point (KNO at 1040 °C, KBNNO1, KBNNO2, and KBNNO3 at 1150 °C, and KBNNO4 and KBNNO5 at 1200 °C, respectively) and sintering the pellets within the same composition matrix. The bulk densities of sintered pellets are calculated through the weights and dimensions of the samples; both the KNO and KBNNO2 ceramics show an above 93% relative density. The ceramics are ground to a final dimension of 10 mm in diameter and 0.5 mm in thickness and then single-side polished and cleaned in pure ethanol with an ultrasonic bath and rinsed several times with ethanol before the spectral measurements.

The crystalline structures of KBNNOx ceramics are investigated by x-ray diffraction (XRD) using a Ni-filtered Cu $K\alpha$ radiation source (D/MAX-2550 V, Rigaku Company). A vertical goniometer (model RINT2000) is used in the XRD measurements, and a continuous scanning mode (θ-2θ) with a scanning rate of 10°/min and an interval of 0.02° is selected. Temperature-dependent Raman scattering measurements are carried out by a micro-Raman spectrometer with a spectral resolution of 1 cm^{-1} (Jobin-Yvon LabRAM HR 800 UV) in the temperature range of 77–793 K with steps of 25 K, and the precision is about 0.5 K. A He-Ne laser with a wavelength of 632.8 nm is taken as the exciting source. The laser beam is focused through a 50× microscope with a working distance of 18 mm. An air-cooled charge coupled device (CCD) (−70 °C) with a 1024 × 256 pixels front illuminated chip was used to collect the scattered signal dispersed on a 1800 grooves/mm grating. All spectra are corrected by the Bose-Einstein temperature factor to facilitate comparison and eliminate the contribution from the Bose-Einstein population factor. The optical absorption experiments are carried out by an ultraviolet-visible-near-infrared (UV-vis-NIR) spectrophotometer (Cary 500, Varian) equipped with an integration sphere. To estimate the band gaps, the Kubelka-Munk (K-M) function given below is calculated, $F(R) = \frac{(1-R)^2}{2R}$, where R is the experimental reflectance referred to in the $BaSO_4$ standard. Hereafter, the K-M function is considered to be proportional to the optical absorption. Hence, the absorption coefficient α can be substituted by $F(R)$ in the Tauc equation $(\alpha h\nu)^n = A(h\nu - E_g) = [h\nu F(R)]^n$, where h is the Planck's constant, ν is the frequency of vibration, E_g is the band gap, and A is the proportional constant, with $n = 2$ for the direct allowed transition, and $n = 1/2$ for the indirect allowed transition. The direct band gap $n = 2$ in KBNNOx FEs is used to precisely calculate the E_g [1,2].

III. RESULTS AND DISCUSSION

A. Structural analysis

Figure 1 illustrates the XRD patterns of KBNNOx ceramics measured at room temperature. The main phase of KNO (JCPDF No. 32-0822) suggests that all KBNNOx samples belong to the orthorhombic phase. A typical peak splitting expected for the end member KNO is clearly observed, but only

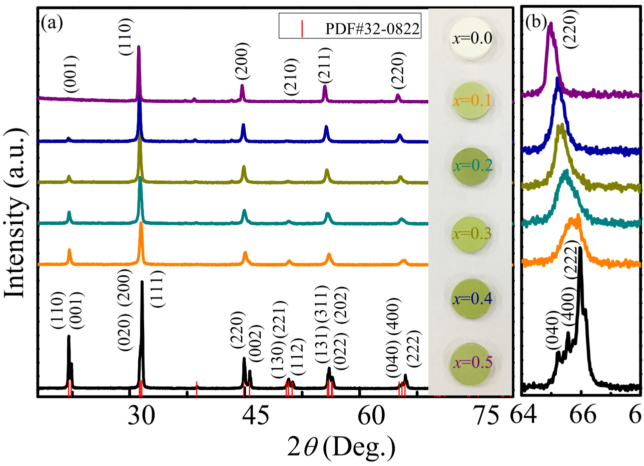

FIG. 1. (a) The XRD patterns and (b) enlarged patterns of the KBNNOx ceramics at room temperature. Note that each spectrum is shifted in intensity for clarity. It also shows the images of the KNO and KBNNOx pellets for $x = 0.1$–0.5 compositions.

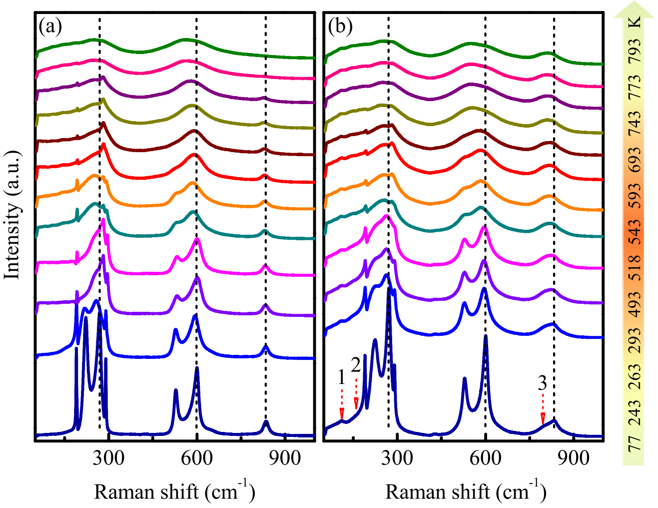

FIG. 3. Temperature-dependent Raman scattering for (a) KNO and (b) KBNNO2 ceramics collected in the temperature range from 77 to 793 K. The arrows are applied to show new phonon modes. For clarity, each spectrum is shifted in intensity.

single peaks are visible for the solid solution KBNNOx. Nevertheless, those single peaks are asymmetric, indicating a clear lattice distortion away from the perfect cubic symmetry. Additionally, reflections shift slightly but systematically towards lower 2θ angles with increasing x, indicating the cosolubility of BNNO and KNO is accompanied by an increasing unit cell volume. Temperature-dependent XRD results are obtained in Fig. 2 and Fig. S1 in the Supplemental Material [27]. The KNO sample shows crystalline structural anomalies, which indicate that rhombohedral (R) $\longrightarrow$ orthorhombic (O) $\longrightarrow$ tetragonal (T) phase transitions occur at 263 and 493 K, respectively [Fig. 2(b)]. By contrast, the peak splitting in the KBNNO2 ceramic is not as distinct as in KNO, whereas the peak position behaviors (see arrows) can be used as a reference for structural evolutions [Fig. 2(d)]. A gradual transition, from $R \rightarrow O \rightarrow T$, with increasing temperature can be clearly observed [28,29]. Indeed, Raman spectra provide strong evidence that KNO and KBNNO2 are isostructural. The average orthorhombic crystal symmetry for KBNNO2 is also confirmed by the Raman data shown in Fig. 3. The typical spectral features exhibited by the FE KNO polymorph are also visible in the Raman spectra for all KBNNO1–KBNNO5 samples, as shown in Figs. S2 and S3 in the Supplemental Material [27]. A spectral similarity is sufficient to simultaneously ascertain the orthorhombic crystal symmetry and the occurrence of long-range polar order in the KBNNOx.

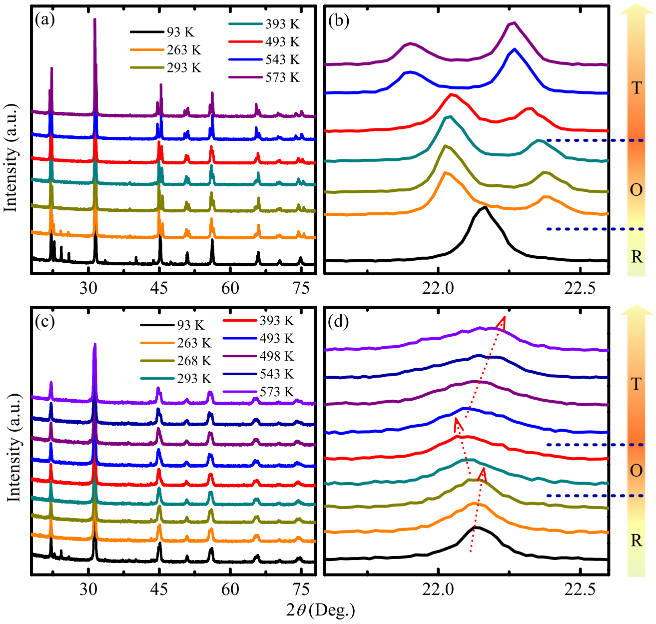

FIG. 2. Temperature-dependent XRD data in (a) end member KNO and (b) solid solution KBNNO2 ceramics at selected temperatures, respectively. Note that the phase transitions are more evident in KNO, but both ceramics show spectral characteristics revealing R-O-T phase transitions.

B. Raman scattering

As a group theoretical analysis predicted in Tables I and II, the end member KNO possesses three acoustic and 12 optical phonons [30]. According to symmetry, three $A_1 + 4E$ are first-order Raman-active optical modes in the rhombohedral ($R3m$, C_{3v}^5) phase with an A_2 phonon mode as Raman silent, four $A_1 + 4B_1 + 3B_2 + A_2$ in the orthorhombic phase of $Amm2$ (C_{2v}^{14}), and three $A_1 + 4E + B_1$ in the tetragonal phase of $P4mm$ (C_{4v}^1). First-order Raman scattering of the three $F_{1u} + F_{2u}$ is forbidden in the centrosymmetric cubic ($Pm\bar{3}m$, O_h^1) phase. The observed modes can be separated into translational modes of an isolated A-site cation and the internal modes of coordination polyhedra. Some attempts have been made to study the connections of the atomic site disorder and the above-mentioned two kinds of modes of the NbO_6 octahedron between R and O, O and T, and T and cubic (C) phases via Raman scattering experiments at different temperatures. Atomic site disorder lowers translational symmetry, effectively relaxing the Raman selection rules. It leads to an enhancement of phonon scattering rates,

TABLE I. Frequencies (cm^{-1}) of the main zone-center modes in the rhombohedral, orthorhombic, tetragonal, and cubic phases for KNO and KBNNO2 ceramics. ^{1}Mixed, ^{2}Mixed, ^{3}Mixed, and ^{4}Mixed represent $(E + A_1)(\mathrm{TO_2,LO_2})$, $(E + B_1)(\mathrm{TO_4,LO_4})$, $E + A_1(\mathrm{LO_3})$, and $B_1 + B_2 + A_1(\mathrm{LO_3})$, respectively. N1, N2, and N3 represent the three new phonons (new1, new2, and new3) caused by doping.

Phases	Phonon modes										
R(KNO)			^{1}Mixed	$E(\mathrm{TO_1})$	$A_1(\mathrm{TO_1})$	^{2}Mixed	$E(\mathrm{TO_3})$		$A_1(\mathrm{TO_3})$		^{3}Mixed
R(KNO)			190.01	222.43	266.27	290.01	529.32		596.59		834.84
77 K			(0.05)	(0.09)	(0.10)	(0.03)	(0.27)		(0.22)		(0.91)
R(KBNNO2)	$^{\mathrm{N1}}$110.15	$^{\mathrm{N2}}$159.24	190.40	224.37	270.24	290.54	530.51		598.74	$^{\mathrm{N3}}$801.22	833.36
77 K	(2.59)	(2.31)	(0.08)	(0.15)	(0.07)	(0.08)	(0.21)		(0.14)	(5.23)	(2.01)
O(KNO)			$(B_1,B_2)(\mathrm{TO_2})$	$B_1(\mathrm{TO_1})$	$A_1(\mathrm{TO_1})$	$A_1(\mathrm{TO_4,LO_4})$	$B_2(\mathrm{TO_3})$	$B_1(\mathrm{TO_3})$	$A_1(\mathrm{TO_3})$		^{4}Mixed
O(KNO)			191.86	222.29	279.57	295.93	532.15	571.00	601.19		833.13
263 K			(0.06)	(2.04)	(0.14)	(0.08)	(0.32)	(1.47)	(0.36)		(0.41)
O(KBNNO2)	$^{\mathrm{N1}}$110.01	$^{\mathrm{N2}}$159.24	192.91	220.33	268.35	290.36	528.75		594.35	$^{\mathrm{N3}}$801.50	832.37
293 K	(0.59)	(0.78)	(0.06)	(1.19)	(0.93)	(0.17)	(0.18)		(0.15)	(2.14)	(1.43)
T(KNO)			$(E + A_1)(\mathrm{TO_2})$	$E(\mathrm{TO_1})$	$A_1(\mathrm{TO_1})$	$E(\mathrm{TO_4,LO_4})$	$E(\mathrm{TO_3})$	$A_1(\mathrm{TO_3})$			^{3}Mixed
T(KNO)			193.67	256.80	280.11	294.42	531.58		587.30		830.67
493 K			(0.10)	(2.69)	(0.58)	(0.49)	(0.53)		(0.36)		(0.57)
T(KBNNO2)	$^{\mathrm{N1}}$110.15	$^{\mathrm{N2}}$159.24.24	194.48	226.51	252.55	283.31	525.33		587.60	$^{\mathrm{N3}}$799.43	831.17
468 K	(0.84)	(0.58)	(0.03)	(3.80)	(1.87)	(1.05)	(0.49)		(0.43)	(2.15)	(1.32)
C(KNO)	$F_{1u}(\mathrm{TO_1})$	$F_{1u}(\mathrm{TO_2})$	$F_{2u}(\mathrm{TO_4})$	$F_{1u}(\mathrm{TO_3})$	$F_{1u}(\mathrm{LO_3})$						
C(KNO)		147.61	261.80	572.64							
773 K		(1.52)	(0.73)	(0.37)							
C(KBNNO2)		147.49	266.40	565.66	809.49						
773 K		(1.56)	(0.99)	(0.59)	(0.71)						

manifesting as a broadened full width at half maximum (FWHM), complicating the determination of peak positions and mode assignments [31–34]. Nevertheless, Raman-active mode assignments and transition temperatures in A-site solid solutions such as $(\mathrm{K},A)\mathrm{NbO_3}$ (A = Na, Li, La) have been made and can also be accomplished in B-site solid solution systems [e.g., $\mathrm{K(Ta_{1-x}Nb_x)O_3}$], based on comparisons with end members [35,36]. Here, we report temperature-dependent Raman scattering in A- and B-site codoped bulk ceramic KBNNOx. In order to confirm the interpretation of Raman spectra in KBNNOx ceramics, polarized Raman spectra were also measured (not shown). The cross (VH), parallel (VV), and nonpolarized Raman spectra do not differ qualitatively except for the intensity variations. It is probably ascribed to the existence of micropolar domains, which partly influence the vibrational properties, as well as the Raman selection rules. For both KNO and KBNNO, polycrystalline samples with the primary contributing modes and the corresponding symmetry assignments in each phase are listed in Table I.

As an example, Figs. 3(a) and 3(b) show the Raman spectra of KNO and KBNNO2 ceramics at different temperatures. Additional stoichiometries are available in the Supplemental Material. Since phonon center positions (PCPs) are temperature dependent, vibrational mode assignment is the most straightforward in low-temperature spectra [Fig. 3(a), R phase]. Furthermore, KNO and KBNNO2 samples are polycrystalline, and the signal measured is an average of many oblique angles. It is not strictly associated with phonon wave vectors, which are neither parallel nor perpendicular to the specific crystallographic axes that would allow for the proper assignment of transverse and longitudinal optical (TO, LO) phonon modes [37]. In the low- and mid-wave-number region, the Raman spectrum of KNO is mainly characterized by (i) a Fano-type interference dip at 190 cm^{-1} due to $(E +$

TABLE II. Correlation, splitting, and degeneracy of the zone-center phonon symmetry for the various structures of KBNNOx. A_2, F_{1u}, and F_{2u} modes are not Raman active.

Rhombohedral	Orthorhombic	Tetragonal	Cubic
$R3m(C_{3v}^5)$	$Amm2(C_{2v}^{14})$	$P4mm(C_{4v}^1)$	$Pm\bar{3}m(O_h^1)$
$3A_1 + 3E$	$3A_1 + B_1 + 3B_2$	$3A_1 + E$	$3F_{1u}$
$E + A_2$	$A_1 + B_1 + A_2$	$B_1 + E$	F_{2u}
$(R \rightarrow O)_{\mathrm{splitting}}$	$(O \rightarrow T)_{\mathrm{formation}}$	$(T \rightarrow C)_{\mathrm{transition}}$	
$E(\mathrm{TO_1}) \rightarrow B_1(\mathrm{TO_1}) + B_2(\mathrm{TO_1})$	$B_1(\mathrm{TO_1}) + B_2(\mathrm{TO_2}) = E(\mathrm{TO_1})$	$A_1(\mathrm{TO_1}) + E(\mathrm{TO_1}) = F_{1u}(\mathrm{TO_1})$	
$E(\mathrm{TO_2,LO_2}) \rightarrow B_1(\mathrm{TO_2,LO_2}) + B_2(\mathrm{TO_2,LO_2})$	$B_1(\mathrm{TO_4,LO_4}) + B_2(\mathrm{TO_4,LO_4}) = E(\mathrm{TO_4,LO_4})$	$A_1(\mathrm{TO_2}) + E(\mathrm{TO_2}) = F_{1u}(\mathrm{TO_2})$	
$E(\mathrm{TO_3}) \rightarrow B_1(\mathrm{TO_3}) + B_2(\mathrm{TO_3})$	$B_1(\mathrm{TO_3}) + B_2(\mathrm{TO_3}) = E(\mathrm{TO_3})$	$A_1(\mathrm{TO_3}) + E(\mathrm{TO_3}) = F_{1u}(\mathrm{TO_3})$	
Heating	$T_{R\text{-}O}$(K)	$T_{O\text{-}T}$(K)	$T_{T\text{-}C}$(K)
KNO	263	493	743
KBNNO2	293	468	693

A_1)(TO_2,LO_2); (ii) a sharp E(TO_1) mode zone centered at 222 cm^{-1}; (iii) a broad A_1(TO_1) mode centered at 266 cm^{-1}; and (iv) another sharp mode ($E + B_1$)(TO_4,LO_4) at 290 cm^{-1}. Because the phonon modes are overlapping, the E(TO_4,LO_4) and B_1(TO_4,LO_4) modes appear to merge as a single peak ($E + B_1$)(TO_4,LO_4). The high-wave-number region (500–850 cm^{-1}) is identified as (v) a E(TO_3) at 529 cm^{-1}; (vi) a A_1(TO_3) at 596 cm^{-1}; and (vii) a mixed low intensity $E + A_1$(LO_3) at 834 cm^{-1}. Note that features (i) and (iv) are believed to be verification for the occurrence of long-range polar order in KNO. At room temperature, upon doping, three new modes emerge in the low- and high-frequency regime, respectively, which can be labeled as 1, 2, and 3. The new modes 1 and 2 present low intensity and broad peaks at ∼107 and ∼170 cm^{-1}, respectively, whereas mode 3 is a shoulder on the low-energy side of the $B_1 + B_2 + A_1$(LO_3) mode in the orthorhombic phase. In the past, the low-frequency modes have been associated with A-O vibrations, in particular, to the translational modes and nm-sized clusters of Ba^{2+}/K^{+} cations, according to the similarity to the single-phase $KNbO_3$-5%Bi(Me, Yb)O_3 thin film [33,38]. Moreover, the $E + A_1$(LO_3) mode becomes broader with increasing BNNO contents, which suggests the emergence of a new mode 3 due to the breathing of the octahedra when the B sites were occupied by different B cations (Nb^{5+} and Ni^{2+}) [38]. The general broadening of the Raman modes from the doped ceramics [Fig. 3(b)] results from increased lattice disorder, which manifests itself by the emergence of Urbach tails in the Tauc plot (Fig. 7).

At low temperature, weak Raman peak shoulders cannot be assigned since they come from the first- or second-order Raman scattering and complicated asymmetric structures of the KNO and KBNNO2 samples. The resonance depth at 200 cm^{-1} and the peak at 830 cm^{-1} have also been identified as signatures of ferroelectricity in KNO-based solid solutions. These features disappeared at higher temperatures, which leads to the conclusion that a ferroelectric-to-paraelectric phase transformation occurred. Some modes in the range of 200–300 and 500–650 cm^{-1} gradually become weaker with increasing temperature and finally disappear or submerge, indicating the reduction of structural distortion and the improvement of symmetry. The mode around 600 cm^{-1} exhibits a slight redshift and the intensity of this major peak reduces with increasing temperature, which can be ascribed to the thermal unit-cell expansion and anharmonic phonon-phonon interactions. As a function of temperature, it can be expressed by the perturbation model, which is written as $\omega(T) = \omega_0 + \Delta\omega_e(T) + \Delta\omega_d(T)$, where $\Delta\omega_e(T) = -\omega_0\gamma \int_0^T [\alpha_a(T) + \alpha_b(T) + \alpha_c(T)]dT$, $\Delta\omega_d(T) = A[1 + 2/(n_1)] + B[1 + 3/(n-1) + 3/(n-1)^2] +$ higher-order terms, $n_1 = \exp(h\omega_0/2K_BT)$, and $n = \exp(h\omega_0/3K_BT)$. The γ is the Grüneisen parameter. The parameters α_a, α_b, and α_c are the thermal expansion coefficients in the a, b, and c axes, respectively. It should be emphasized that the first term ω_0 represents the harmonic frequency of the optical mode and the second one is related to the thermal expansion of the lattice [39]. Moreover, the third one corresponds to cubic, quadratic, and higher-order anharmonic coupling between phonons. Therefore, the redshift of mode frequency with increasing temperature is mainly due to the thermal expansion [40]. The relaxed structures are used to analyze the cation displacements, which can be adapted to evaluate the effect of the BNNO substitution on the local structure and to estimate the polarization by multiplying the cation displacements by their respective Born effective charge (Z^*) values [41]. In addition, the low-frequency shifting, the weakening, and the disappearance of Raman modes against temperature can also suggest a symmetry change [42–44].

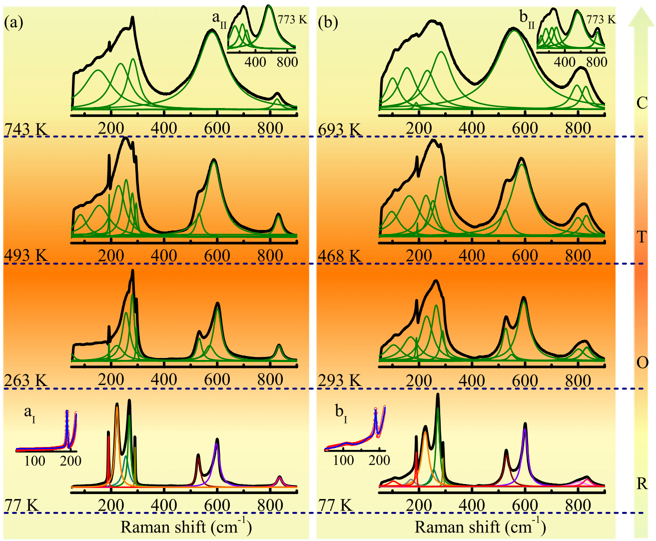

FIG. 4. Raman spectra of (a) KNO and (b) KBNNO2 ceramics at selected temperatures after correcting for the thermal population factor and the corresponding Breit-Wigner-Fano line as well as multi-Lorentz peak fitting at selected temperatures. The insets a_I and b_I show the best fit with the BWF line at around 190 cm^{-1}. Mode behaviors are clearly observed through structural and ferroelectric phases.

To facilitate the explanation of temperature evolution and understand the correlation of interior structural changes and Raman modes, all Raman experimental spectra are decomposed into a series of bands with the multi-Lorentzian oscillator approximation and Breit-Wigner-Fano (BFW) asymmetry. Notably, all measured Raman spectra are corrected for the Bose-Einstein temperature factor in the fitting process to eliminate the contribution of the Bose-Einstein population factor from the measured scattering intensity. Meanwhile, the BWF line shape at 190 cm^{-1} is defined by the following formula, $I_{BWF}(\omega) = I_0(1 + s/q_{BWF})^2/(1 + s^2)$, where $s = (\omega - \omega_{BWF})/\Gamma$ [45,46]. Here ω, ω_{BWF}, $1/q_{BWF}$, Γ, and I_0 are the Raman shift, the spectral peak position, the asymmetric factor, the spectral width, and the maximum intensity of the BWF spectra, respectively. For the finite linewidth case (at around 190 cm^{-1}), there is an excellent agreement with the experimental data in the insets a_I and b_I of Fig. 4. By fitting the Raman spectra with Lorentzian and BFW lines, some typical temperature-dependent phonon frequencies and intensity behaviors are extracted at selected temperatures in Figs. 4(a) and 4(b). From Figs. 4(a) and 4(b), it is apparent that the typical modes for B_1(TO_1) (∼221 cm^{-1}) and A_1(TO_1) (∼256 cm^{-1}) show an obvious blueshift and FWHM broadening beyond about 263 K for KNO. Instead, for the KBNNO2 sample, B_1(TO_1) (∼228 cm^{-1}) and A_1(TO_1) (∼264 cm^{-1}) modes remain at the PCP, but beyond that the resonance depth at ∼250 cm^{-1} disappears at 293 K. It can be ascribed to

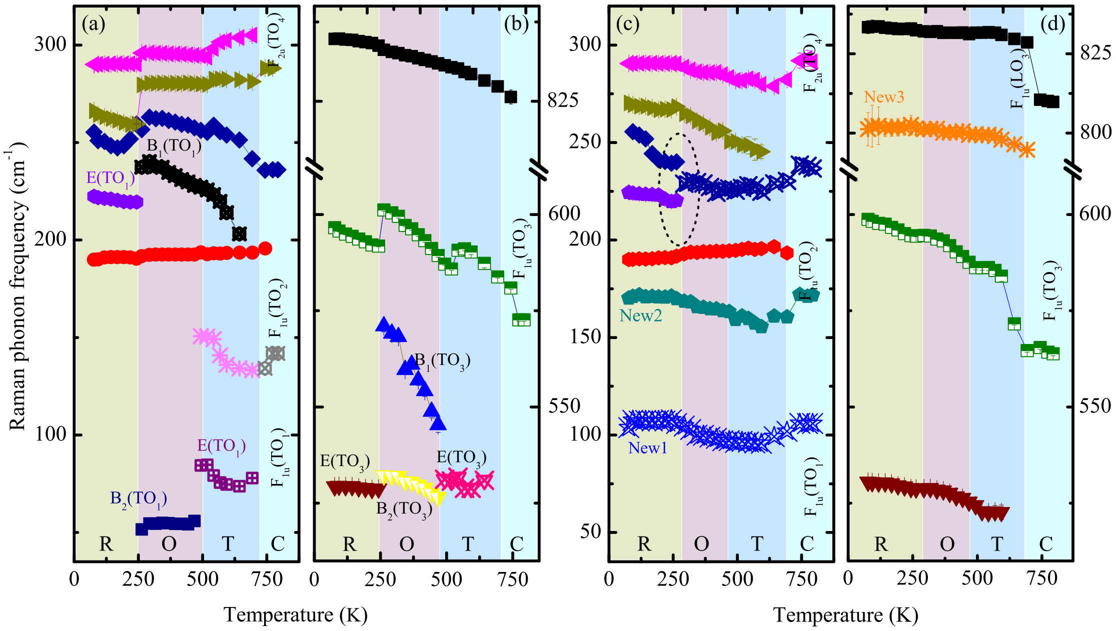

FIG. 5. Temperature dependence of the phonon frequency from the end member KNO and solid solution KBNNO2 ceramics. (a), (c) The low-frequency range of 50–320 cm^{-1}, and (b), (d) the high-frequency range of 520–840 cm^{-1}. Note that different shaded regions indicate that the ceramics are located in diverse phases.

the thermal expansion of the lattice and anharmonic phonon-phonon interactions as mentioned above. However, the abnormal phonon redshift of $E(\mathrm{TO}_1)$ ($\sim$256 cm^{-1}) and $A_1(\mathrm{TO}_3)$ ($\sim$280 cm^{-1}) from 418 to 493 K for KNO and 318 to 468 K for KBNNO2 cannot be only explained by the temperature effect, which may illustrate that there is one relaxation mode during the phase transformation. In other words, a polymorphic phase transition (PPT) between the O and T phases is found for KNO and KBNNO2 in the temperature range from 418 to 493 K and 318 to 468 K, respectively. Note that the PPT is obtained distinctly from the experimental spectra in Figs. 3(a) and 3(b). Additionally, the spectral features across the T-C phase transition boundary are also evident. The frequency from all phonon modes except that of $A_1(\mathrm{TO}_1)$ shift to lower wave numbers and the intensities of all major peaks reduce with increasing temperature. Just below the transition, the T phase has strong broad modes at $\sim$250 and $\sim$580 cm^{-1} and weaker modes at 192, 530, and 830 cm^{-1} for KNO. The two strong modes have broadened above $T_{T\rightarrow C,\mathrm{KNO}} \approx 743$ K. At this temperature, these weak modes that give a signal above the background have decreased or vanished, as expected from previous studies of the mode evolution in KNO [47]. However, it is worth noting that the aforementioned new modes 1, 2, and 3 are always present at $T_{T\rightarrow C,\mathrm{KBNNO2}} \approx 693$ K for KBNNO2. Through this transition temperature, the mode at $\sim$587 cm^{-1} condenses into the mode at $\sim$525 cm^{-1} to become a single mode at high temperatures for both KNO and KBNNO (Fig. 4). With the discussion above, we can conclude that KNO and KBNNO2 ceramics undergo the same sequence of phase transitions with increasing temperature, from an R-phase fully ordered solid, to a partly disordered O phase, T phase, and finally to a disordered C solid.

In order to obtain a clear description of the dynamical properties from the successive phase transitions, here, we assume that the 12 optical vibration phonon modes transform as the $3F_{1u} + F_{2u}$ irreducible representation in the C phase. The three F_{1u} phonons are labeled as 1, 2, and 3 in order of increasing frequency and the F_{2u} phonon is labeled as 4. It is useful to know the classification of the optical modes (refer to Table I) and their correlation to the zone-center phonon symmetry in the various structures; the splitting and creation of degenerate modes on heating are recalled in Table II [48–53].

For simplicity, the zone centers of the main modes in each phase are plotted in Figs. 5(a)–5(d) against the temperature between 77 and 793 K. Changes in the frequency shift are clear at the $R \rightarrow O$, $O \rightarrow T$, and $T \rightarrow C$ boundaries. On approaching the transition temperature from below, the KNO and KBNNO2 samples observed a slight softening and damping with increasing temperature, exactly as expected to follow from the lattice thermal expansion. The $R \rightarrow O$ transition temperature for KNO is determined using the anomalous hardening of $B_1(\mathrm{TO}_1)$ ($\sim$250 cm^{-1}), $A_1(\mathrm{TO}_1)$ ($\sim$270 cm^{-1}), and $A_1(\mathrm{TO}_3)$ ($\sim$570 cm^{-1}) modes and the sudden appearance of the $B_1(\mathrm{TO}_3)$ mode as a shoulder on the low-energy side for the $A_1(\mathrm{TO}_3)$ mode at the $R \rightarrow O$ transition temperature $T_{R\rightarrow O} \approx 263$ K (Table II). Those phenomena are interpreted by the peak splitting of the degenerate E component according to the transfer equation $(R \rightarrow O)_{\mathrm{splitting}}$, as shown in Table II. When the unit cell contains several NbO$_6$ octahedra with different symmetries, splitting can be observed, resulting from different crystal fields and extra conditions [i.e., temperature, pressure, cross (VH), parallel (VV), and nonpolarized] in the site symmetries. This transition corresponds to the onset of disorder along the y direction of the pseudocubic cell. Therefore, the symmetric stretching mode of $A_1(\mathrm{TO}_1)$ demonstrates a unique change in its wave-number shift as well as in its full width at half maximum (FWHM). Note that there is an interference dip at $\sim$190 cm^{-1} for Raman spectra in the O phase. For the KBNNO2 sample, modes at ~100, ~190, ~220, ~250, and ~270 cm^{-1} also exhibited abrupt changes at $T_{R\to O}$ ~ 293 K (Table II). By contrast with KNO, the modes of $B_1(\mathrm{TO}_1)$ and $B_2(\mathrm{TO}_1)$ in the KBNNO2 disappear at the $R \to O$ phase boundary. It is ascribed to the mode competitions between new1 and $B_2(\mathrm{TO}_1)$. Although the temperature-dependent frequency shifts are not as distinct as in KNO, the behaviors of the end member can be used as a reference for mode assignment and to extract the phase transition temperatures for KBNNO2.

In the O phase, the dynamic behavior is dominated by the soft phonon $B_2(\mathrm{TO}_1)$ and the hard $B_1(\mathrm{TO}_3)$ and $B_2(\mathrm{TO}_3)$ modes. The $O \to T$ transition temperature for KNO (493 K) is also established from the behavior of the modes mentioned above. At the $O \to T$ phase boundary, the intensities of the broadband assigned to $A_1(\mathrm{TO}_1) \oplus B_1(\mathrm{TO}_1)$ at ~280 cm^{-1} and of the $(B_1, B_2)\mathrm{TO}_2$ mode at ~200 cm^{-1} were found to decrease while the background level below ~100 cm^{-1} increased. This was assigned to the negative frequency jump of the $B_1(\mathrm{TO}_1)$ mode with a strong damping at low frequency leading to the formation of the degenerate $E(\mathrm{TO}_1)$ mode; the other degenerate modes are created around ~280 and ~520 cm^{-1}. These formations of the degenerate can be explained using the transfer equation $(O \to T)_{\mathrm{formation}}$ from Table II. The determination of this transition temperature from KBNNO2 is based on other modes, such as the combination of vibrational modes at ~290 cm^{-1}. A weighted error analysis is performed using standard expressions for the probability distribution and weighting factors. This effectively removes the contributions of the modes at ~290 cm^{-1} by weighing them by the inverse of their variance such that they do not significantly affect the transition temperature of KBNNO2. Besides the above-mentioned prototypical features, the anomalies of the modes around 230 cm^{-1} in the KBNNO2 sample at a temperature of 468 K may be due to changes in the domain microstructure. Another key determination of this transition temperature $T_{O\to T} \approx 468$ K is ascertained from the distinct frequency shifts of $A_1(\mathrm{TO}_1)$ and $E(\mathrm{TO}_1)$ [from the degenerate modes of $B_1(\mathrm{TO}_1) + B_2(\mathrm{TO}_1)$]. Specifically, the modes at ~530 and ~600 cm^{-1} are useful for both the KNO and KBNNO samples and are significant for determining the $O \to T$ transition [Figs. 5(b) and 5(d)].

The $T \to C$ transition is located around $T_{T\to C} \approx 743$ K for KNO and 693 K for KBNNO2, where $T_{T\to C} \leqslant T_C$ (Curie temperature). The approach of the transition is characterized by a strong increase of the background signal below 300 cm^{-1} due to the damping in the region of the $E(\mathrm{TO}_1)$ mode and the condensation of the $A_1(\mathrm{TO}_1)$ mode for the KNO and KBNNO2 samples. By reference to $(T \to C)_{\mathrm{transition}}$ (Table II), this feature corresponds to the transition $A_1(\mathrm{TO}_1) + E(\mathrm{TO}_1) \to F_{1u}$. Additionally, as we can see in Figs. 5(a) and 5(b), except that the $E(\mathrm{TO}_1)$ mode ~190 cm^{-1} and the $E + A_1(\mathrm{LO}_3)$ mode ~830 cm^{-1} disappear, which can be caused by the bending of NbO_6, the remaining hard modes are degenerated into $F_{1u}(\mathrm{TO}_2)$, $F_{2u}(\mathrm{TO}_4)$, and $F_{1u}(\mathrm{TO}_3)$ at ~150, ~260, and ~570 cm^{-1}, respectively. For KBNNO2, $F_{1u}(\mathrm{TO}_2)$, $F_{2u}(\mathrm{TO}_4)$, $F_{1u}(\mathrm{TO}_3)$, and $F_{1u}(\mathrm{LO}_3)$ at ~150, ~270, ~560, and ~810 cm^{-1} are observed in the C phase [Figs. 5(c) and 5(d)]. Following the symmetry selection rules, no first-order Raman scattering should be obtained. However, some broadening bands (i.e., around 280 cm^{-1} for KN, and around 105 and 288 cm^{-1} for KBNNO2) still appear in the C phase due to the disorder of the central ion (Nb^{5+}), as can be see from the insets $\mathrm{a_{II}}$ and $\mathrm{b_{II}}$ of Fig. 4, which breaks the crystal inversion symmetry of the O_h point group. The experimental result also shows an unexpected persistence for $A_1(\mathrm{TO}_1)$ until 30 K above $T_{T\to C}$, which can be attributed to the existence of a precursor order or ferroelectric clusters near the transition [54,55]. Thus, the precursor-order process is observed in the case of a zone-center instability in KBNNO2. Therefore, Raman scattering constitutes an efficient probe of ordering manifestations occurring near the structural phase transition. It can reveal deviations from the expected group theory predictions for the normal modes, which are Raman inactive above $T_{T\to C}$ but Raman active below [56].

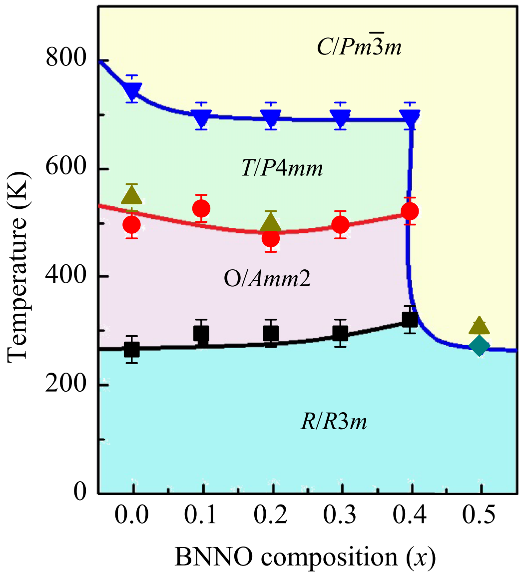

FIG. 6. Phase diagram of KBNNOx ceramics with different BNNO compositions. The phase transformation temperatures in the present work are marked with the symbols (square for $R \to O$, solid circle for $O \to T$, and triangle down for $T \to C$) and the values marked by the symbol (triangle) are from the present XRD data in Fig. 2 and Fig. S1. Additional phase transition temperature (marked by lozenge) available in Ref. [3].

C. Phase diagram

Combining with an XRD and Raman data analysis, a phase diagram of KBNNOx has been extracted. Figure 6 includes the present results and earlier studies of KBNNOx ceramics [3]. Inspection of Fig. 6 shows that there is a nonmonotonic change in the transformation temperature of $O \to T$ and $T \to C$ with BNNO fraction, with an initial steep decay for a low BNNO fraction and then a slow rise starting from $x = 0.2$. To explain the above phenomenon, density functional theory (DFT) calculations are performed for P values in KNO ($0.43\ \mathrm{C\,m^{-2}}$) and KBNNO3 ($0.2\ \mathrm{C\,m^{-2}}$), indicating that BNNO substitution decreases polarization and reduces the temperature of the ferroelectric→ferroelectric and ferroelectric→paraelectric transitions [1]. The DFT finding of a distribution for Nb displacement magnitudes and variation in the local structure is consistent with broadening in both

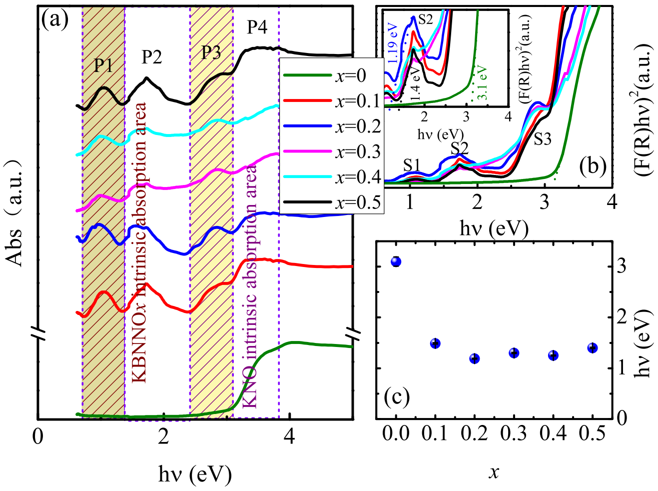

FIG. 7. (a) UV-vis-NIR absorption spectra of the KBNNOx ($x =$ 0–0.5) ceramics. (b) Tauc plot of $(\alpha h\nu)^2$ vs $h\nu$ for the absorption spectra and for enlarged pattern (inset). (c) Band-gap values vs BNNO compositions (from shoulder2). Note that P1, P2, P3, and P4 represent the absorbance peak1, peak2, peak3, and peak4, respectively. S1, S2, and S3 represent three new absorbance shoulders (shoulder1, shoulder2, and shoulder3), respectively.

the dielectric [3] and Raman data (this work). Especially, the temperature evolution of the Raman shift used to assign the $T \to C$ transition temperature changes from an abrupt drop at T_C observed for KNO, to a gradual decrease to a constant value observed for KBNNOx. On the other hand, the Raman measurements are sensitive to the variation in the local structure, where some local environments exhibit enhanced 0 K displacements that are likely to persist to higher temperatures than the ferroelectric structure in the parent KNO material [3]. Therefore, it is reasonable to consider the anomalies of the phonon and central peak shift with temperature as a determination of the ferroelectric→paraelectric phase transformation at about 743 K for KNO and 693 K for KBNNOx. Nevertheless, it is clear that the $O \to T$ transformations extracted from temperature-dependent XRD and Raman spectra are not at the same point for KNO and KBNNO2 samples in Fig. 6. This can be attributed to the unstable phase structure and experimental temperature step of 25 K, which can induce the above errors. Based on the above study, a detailed phase diagram is presented here. This is not only helpful in understanding other photovoltaic (PV) phase transition mechanisms that relate to the local structure evolution with temperature, but also provides guidelines for the design and optimization of PV materials.

D. Optical absorption and photocatalytic property

Figure 7(a) shows the light-absorption properties of the KNO and KBNNOx ceramics using a UV-vis-NIR spectrophotometer. We find that the Ni-containing KBNNOx solutions exhibit multiabsorbance peaks (e.g., P1, P2, P3, and P4). It is important to indicate that these solid solutions not only have very broad absorption in the UV-vis light range, but also possess remarkable absorption to NIR compared with other reported semiconductors including the hottest perovskite sensitizer $CH_3NH_3PbI_3$. The significant NIR absorption is attributed to oxygen vacancies produced by the existence of Ni^{2+} which is similar to $Pb(Ti_{1-x}Ni_x)O_{3-x}$ solid solutions. This result is significant in fully utilizing the solar energy exploring the potential applications in NIR-related fields. The existence of oxygen vacancies also indicates that KBNNOx is an n-type oxide semiconductor as with other most widely studied oxide semiconductors.

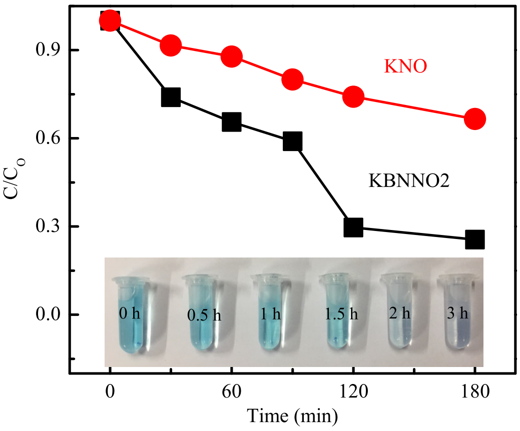

FIG. 8. Photocatalytic decoloration of methylene blue (MB) under visible light with (lower) and without (upper) KBNNO2 powders. Inset: Color evolution of MB at the corresponding irradiation time.

The band gaps of all compositions were determined using the Tauc plots in Fig. 7(b). Currently, there is no information about the number and location of the band-gap edges for the full spectrum of the KBNNOx materials. Here, Fig. 7(b) shows three new shoulders (S1, S2, and S3) presented in all doped materials. As an example for S2 in the inset, the corresponding band-gap energies were obtained from the intercept of the tangent line in the plot of $[F(R)h\nu]^2$ versus energy, whose magnitude decreases first and then increases with increasing x [Fig. 7(c)]. For KBNNO2, the extracted band gap is 0.7, 1.2, and 2.4 eV, respectively, consistent with the first-principles calculation results for direct band gaps of 1.49 and 1.84 eV. Furthermore, these values are much lower than the 3.1 eV band gap of the KNO ceramics (Fig. 7). Owing to the band gap from S2 matching well with the $E_g \sim 1.5$ eV for the solar spectral center, the KBNNOx materials can provide great potential applications to photocatalysts and photovoltaics.

Further evidence of photon-generated carriers in KBNNOx came from photocatalytic activity. The UV-light source is a 500-W-long arc Hg lamp equipped with a filter, which only allows UV light through. Under UV-light illumination, methylene blue (MB) dye was reduced to 30% of its initial concentration ($C_0 \sim 1 \times 10^{-5}$ mol L^{-1}) in the presence of KBNNO2 powders compared to less than 75% if without, as can be seen in Fig. 8. The increased degradation may be attributed to an electron donation from KBNNO2 as a photocatalyst. Together, these results leave no doubt that there are robust photoelectric effects in polar, orthorhombic KBNNO2.

E. Physical mechanism

To elucidate the origin of the band-gap vibration that accompanied the phase transformation in ferroelectric materials, a first-principles calculation is utilized. Within the resource

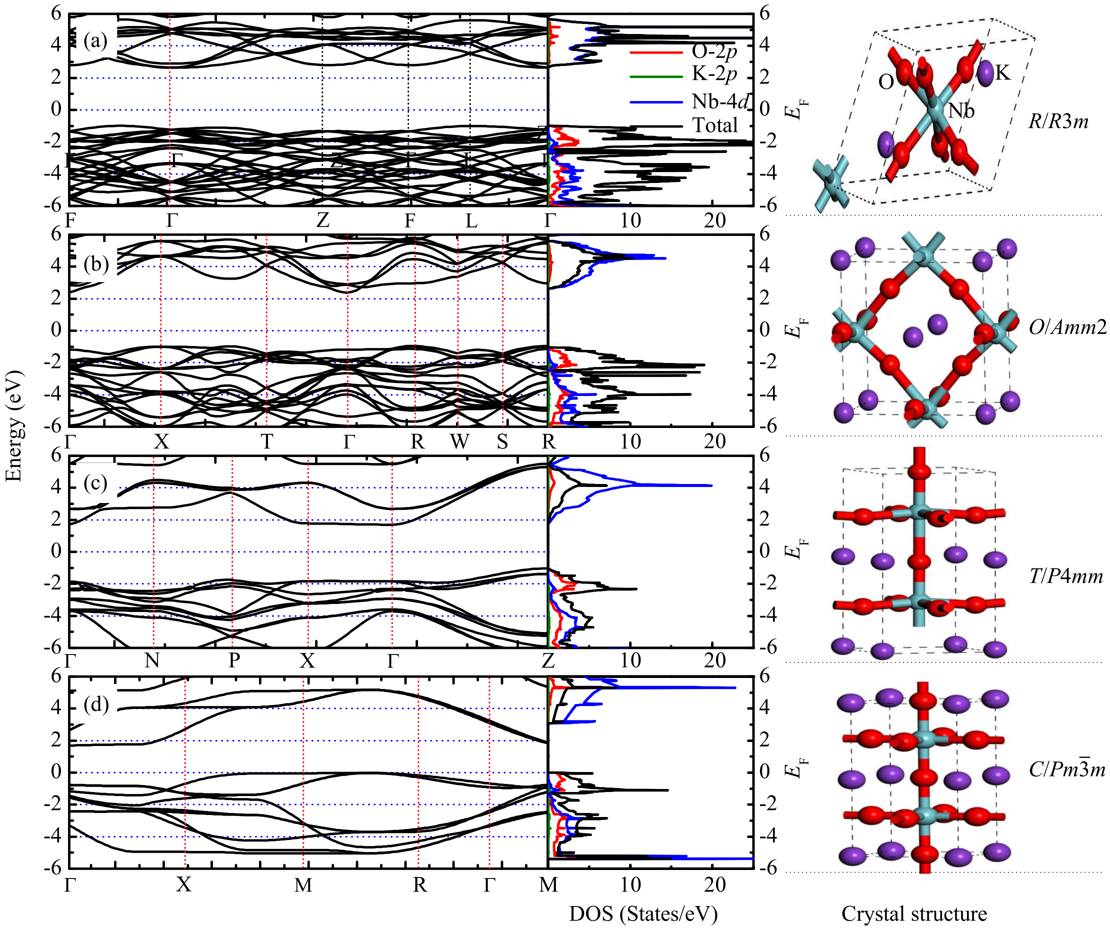

FIG. 9. Crystal structure, calculated band structure, and corresponding density of states for (a) rhombohedral, (b) orthorhombic, (c) tetragonal, and (d) cubic KNbO$_3$.

limits of the technique, the theoretical calculations are carried out only for KNO to simplify the calculations. The hybrid functional of Heyd, Scuseria, and Ernzerhof (HSE06) is used to corroborate the band-gap change trend [57–59]. The cutoff of plane-wave energy is determined to be 500 eV. The structure transitions of KNO can be described by the *R* phase in space group *R*3*m* at low temperature, the *O* phase in space group *Amm*2 near 263 K, the *T* phase in space group *P*4*mm* at 493 K, and the paraelectric *C* structure in space group $Pm\bar{3}m$ above 743 K. Structural optimizations are performed for the four phases and the ions are fully relaxed toward equilibrium until the residual forces on each atom are less than 0.03 eV/Å. The corresponding crystal structures, band structure, partial/total density of states (DOS), and equilibrium lattice parameters are presented in Fig. 9 and Table III, respectively. As shown in Figs. 9(a)–9(d), the *R*3*m* structure can be transformed into an *Amm*2 structure caused by both the rotations of the NbO6 octahedra and the displacement of atoms along the *a* axis from Fig. 9. In the ferroelectric *P*4*mm* phase, the distortion of NbO$_6$ octahedra is decreasing. Moreover, the movement of the O atoms weakens the tilt about the *c* axis. There are no tilt and rotations of the NbO$_6$ octahedra in the $Pm\bar{3}m$ cubic structure, ensuring the structural symmetry of the body-centered-cubic system. The top of the valence bands and the bottom of the conduction ones consist of mainly O 2*p* and Nb 4*d* states, respectively [60,61]. The direct electronic transition of the optical band gap is about 3.63 eV for the *R* phase, 3.44 eV for the *O* phase, 2.73 eV for the *T* phase, and 2.64 eV for the paraelectric phase, respectively. A detailed analysis shows that the band gap of KNO increases significantly when the structure changes from the *C* phase to the distorted *R* phase, because of the correlation between the NbO$_6$ octahedral distortion, Nb ion off-center displacements, and the electronic structure [13,62,63]. It is apparent that a more isotropic lattice distortion in the *R* phase reduces the splitting between the d_{xy} and $d_{xz/yz}$ orbitals. Altogether, the difference in the electronic band-gap structures is ascribed to their different structural properties.

TABLE III. Optimized lattice parameters of KNO for *R*3*m*, *Amm*2, *P*4*mm* and $Pm\bar{3}m$.

	a (Å)	*b* (Å)	*c* (Å)	*V* (Å^3)
*R*3*m*	4.09	4.09	4.09	68.42
*Amm*2	4.02	4.13	4.13	68.55
*P*4*mm*	4.03	4.03	4.22	68.47
$Pm\bar{3}m$	4.06	4.06	4.06	66.80

Similarly, for Ni-containing KBNNO*x* samples, the structural vibrations are embodied in the degree of combined distortion, which involves the tilts of BO_6 octahedra and the displacement of B-site atoms in the octahedra [64,65]. Grinberg first studied the connection between the electronic structure and noncentrosymmetric material's structure in theory [1]. The theoretical results for KBNNOx materials in the O phase suggest that there are two stable supercell structures for the oxygen vacancies (Ni-V_o-Nb and Ni-V_o-Ni), which correspond to the new absorbances P2 and P3 in Fig. 7(a). The interband transitions of the absorption edges are derived from the hybridized Ni $3d$/O $2p \rightarrow$ Nb $4d$ transition. The reason for the band-gap lowering for KBNNOx ceramics is the orbital splitting. The d orbitals of the B cation split into triply degenerate t_{2g} and doubly degenerate e_g states. For the NiO_6 complex (corresponding to P3), since the Nb^{5+} ion is strongly ferroelectric, its off-center displacement leads to a concurrent change in the Ni-O distance along the z direction [2]. It induces additional splitting between the d_z^2 and $d_{x^2-y^2}$ orbitals of the e_g state and between the d_{xy} and $d_{xz/yz}$ orbitals of the t_{2g} state, whereas for the NiO_5 complex (corresponding to P2), the removal of one O atom at the apical site provides space for the O atom at the opposite site to move away from the central Ni atom. Correspondingly, the Ni-O distance along the Cartesian z direction is much larger than that in the xy plane. Compared to the distorted NiO_6 environment, the splitting between the d_z^2 and $d_{x^2-y^2}$ orbitals is much larger for the NiO_5 complex. As a result, the energy of the d_z^2 orbital in the NiO_5 complex is much lower than that in the NiO_6 complex. Therefore, the study of the electronic band structure can be used as a reference for the band-gap engineering and an understanding of the photovoltaic mechanisms in different phases [13]. In principle, the variations of electronic transitions from first-principle calculations can also be applied to judge the lattice distortions in ferroelectric materials.

IV. CONCLUSIONS

In conclusion, a strategy is proposed to successfully engineer the band gaps of lead-free ferroelectric KBNNOx ceramics with macrovisible light absorbed, supported by optical evidence and first-principles calculations. We find that the band gaps of the innovative materials can be substantially reduced by as much as 1.9 eV through a modification of Ba and Ni cosubstitution. Rigorous Raman peak fittings of spectra collected from KBNNOx and KNO indicate structural and ferroelectric phase transformation temperatures that are close to those for the KNO despite the inclusion of 5–25 at. % of ferroelectrically inactive Ni cations. Taken together with the previous calculations about the variations in atom displacements, local/averaged polarizations, and the absence of frequency dispersion in the dielectric permittivity, these results demonstrate the persistence of ferroelectric ordering in KBNNOx to temperatures that approach the T_C of the KNO. It is more conducive to understanding the photovoltaic mechanisms that relate to the ferroelectric phase. Moreover, the appearance of three new optical phonon modes and differences in the lattice dynamics in KBNNOx, as compared with KNO in different phases, highlights the local and nonlocal characteristics between the two samples. Finally, robust photocatalytic activity on methylene blue is found, which suggests promising applications as photocatalytic degradation, solar absorber layers, and carrier separators in practical photovoltaics. This discovery is also important for the emerging field of ferroelectric photovoltaics as a photocatalyst and visible-light-absorbing strongly ferroelectric materials.

ACKNOWLEDGMENTS

One of the authors (C.Q.L.) would like to thank Prof. A. M. Rappe and Dr. A. Y. Cui for constructive discussions. This work was financially supported by National Key Research and Development Program of China (Grant No. 2017YFA0303403), Natural Science Foundation of China (Grants No. 61674057, No. 61504156, and No. 61227902), Projects of the Science and Technology Commission of Shanghai Municipality (Grant No. 15JC1401600), and the Program for Prof. of Special Appointment (Eastern Scholar) at Shanghai Institutions of Higher Learning and the Fundamental Research Funds for the Central Universities.

---

[1] I. Grinberg, D. V. West, M. Torres, G. Gou, D. M. Stein, L. Wu, G. Chen, E. M. Gallo, A. R. Akbashev, P. K. Davies, J. E. Spanier, and A. M. Rappe, Nature (London) **503**, 509 (2013).
[2] F. G. Wang and A. M. Rappe, Phys. Rev. B **91**, 165124 (2015).
[3] B. Q. Song, X. J. Wang, C. Xin, L. L. Zhang, B. Song, Y. Zhang, Y. Wang, J. Wang, Z. G. Liu, Y. Sui, and J. K. Tang, J. Alloys Compd. **703**, 67 (2017).
[4] W. L. Zhou, H. M. Deng, P. X. Yang, and J. H. Chu, Appl. Phys. Lett. **105**, 111904 (2014).
[5] J. Kreisel, M. Alexe, and P. A. Thomas, Nat. Mater. **11**, 260 (2012).
[6] T. Choi, S. Lee, Y. Choi, V. Kiryukhin, and S.-W. Cheong, Science **324**, 63 (2009).
[7] D. Cao, C. Wang, F. Zheng, W. Dong, L. Fang, and M. Shen, Nano Lett. **12**, 2803 (2012).
[8] W. S. Choi, M. F. Chisholm, D. J. Singh, T. Choi, G. E. Jellison, Jr., and H. N. Lee, Nat. Commun. **3**, 689 (2012).
[9] A. A. Grekov, M. A. Malitskaya, V. D. Spitsina, and V. M. Fridkin, Kristallografiya **15**, 500 (1970).
[10] A. M. Glass, D. von der Linde, and T. J. Negran, Appl. Phys. Lett. **25**, 233 (1974).
[11] V. Belincher and B. Sturman, Phys. Usp. **23**, 199 (1980).
[12] B. Sturman and V. Fridkin, *The Photovoltaic and Photorefractive Effects in Noncentrosymmetric Materials* (Gordon and Breach, Philadelphia, 1992).
[13] F. G. Wang, I. Grinberg, and A. M. Rappe, Phys. Rev. B **89**, 235105 (2014).
[14] G. H. Zhang, H. Wu, G. B. Li, Q. Z. Huang, C. Y. Yang, F. Q. Huang, F. H. Liao, and J. H. Hua, Sci. Rep. **3**, 1265 (2013).
[15] S. Y. Yang, J. Seidel, S. J. Byrnes, P. Shafer, C.-H. Yang, M. D. Rossell, P. Yu, Y.-H. Chu, J. F. Scott, J. W. Ager, L. W. Martin, and R. Ramesh, Nat. Nanotechnol. **5**, 143 (2010).
[16] J. W. Bennett, I. Grinberg, and A. M. Rappe, J. Am. Chem. Soc. **130**, 17409 (2008).

[17] G. Y. Gou, J. W. Bennett, H. Takenaka, and A. M. Rappe, Phys. Rev. B **83**, 205115 (2011).

[18] F. Wang, S. M. Young, F. Zheng, I. Grinberg, and A. M. Rappe, Nat. Commun. **7**, 10419 (2016).

[19] T. Qi, I. Grinberg, and A. M. Rappe, Phys. Rev. B **83**, 224108 (2011).

[20] J. W. Bennett, I. Grinberg, P. K. Davies, and A. M. Rappe, Phys. Rev. B **82**, 184106 (2010).

[21] B. Kundys, Appl. Phys. Rev. **2**, 011301 (2015).

[22] X. Lv, J. G. Wu, S. Yang, D. Q. Xiao, and J. G. Zhu, ACS Appl. Mater. Interfaces **8**, 18943 (2016).

[23] X. P. Wang, J. G. Wu, D. Q. Xiao, J. G. Zhu, X. J. Cheng, T. B. Zheng, Y. Zhang, X. J. Lou, and X. J. Wang, J. Am. Chem. Soc. **136**, 2905 (2014).

[24] X. P. Wang, J. G. Wu, D. Q. Xiao, X. J. Cheng, T. B. Zheng, Y. Zhang, X. J. Lou, and J. G. Zhu, J. Mater. Chem. A **2**, 4122 (2014).

[25] K. Wang, F. Z. Yao, W. Jo, D. Gobeljic, V. V. Shvartsman, D. C. Lupascu, J. F. Li, and J. Rödel, Adv. Funct. Mater. **23**, 4079 (2013).

[26] K. Wang and J. F. Li, Adv. Funct. Mater. **20**, 1924 (2010).

[27] See Supplemental Material at http://link.aps.org/supplemental/10.1103/PhysRevB.97.094109 for temperature-dependent x-ray diffraction measurements and temperature-dependent Raman scattering measurements.

[28] K. Wang and J. F. Li, Appl. Phys. Lett. **91**, 262902 (2007).

[29] B. P. Zhang, J. F. Li, K. Wang, and H. L. Zhang, J. Am. Ceram. Soc. **89**, 1605 (2006).

[30] A. V. Postnikov and G. Borstel, Phys. Rev. B **50**, 16403 (1994).

[31] N. Klein, E. Hollenstein, D. Damjanovic, H. J. Trodahl, N. Setter, and M. Kuball, J. Appl. Phys. **102**, 014112 (2007).

[32] A. Bartasyte, J. Kreisel, W. Peng, and M. Guilloux-Viry, Appl. Phys. Lett. **96**, 262903 (2010).

[33] L. Luisman, A. Feteira, and K. Reichmann, Appl. Phys. Lett. **99**, 192901 (2011).

[34] I. S. Golovina, V. P. Bryksa, V. V. Strelchuk, I. N. Geifman, and A. A. Andriiko, J. Appl. Phys. **113**, 144103 (2013).

[35] H. J. Trodahl, N. Klein, D. Damjanovic, N. Setter, B. Ludbrook, D. Rytz, and M. Kuball, Appl. Phys. Lett. **93**, 262901 (2008).

[36] E. Buixaderas, D. Nuzhnyy, I. Gregora, S. Kamba, M. Berta, B. Malic, and M. Kosec, IEEE Trans. Sonics Ultrason. **56**, 1843 (2009).

[37] R. Loudon, Adv. Phys. **13**, 423 (1964).

[38] C. Pascual-Gonzalez, G. Schileo, and A. Feteira, Appl. Phys. Lett. **109**, 132902 (2016).

[39] Q. Li, J. Wang, M. Li, S. Guo, J. Zhang, Z. Hu, Z. Zhou, G. Wang, X. Dong, and J. Chu, Phys. Rev. B **96**, 024101 (2017).

[40] C. B. Long, H. Q. Fan, and P. R. Ren, Inorg. Chem. **52**, 5045 (2013).

[41] C. J. Hawley, L. Y. Wu, G. Xiao, I. Grinberg, A. M. Rappe, P. K. Davies, and J. E. Spanier, Phys. Rev. B **96**, 054117 (2017).

[42] J. Z. Zhang, K. Jiang, Z. Y. Zhou, Z. G. Hu, G. S. Wang, X. L. Dong, and J. H. Chu, J. Am. Ceram. Soc. **99**, 3610 (2016).

[43] H. C. Gupta, Archana, and V. Luthra, Vib. Spectrosc. **56**, 235 (2011).

[44] H. C. Gupta, Archana, and V. Luthra, J. Mol. Struct. **984**, 204 (2010).

[45] E. H. Hasdeo, A. R. T. Nugraha, M. S. Dresselhaus, and R. Saito, Phys. Rev. B **90**, 245140 (2014).

[46] U. Fano, Phys. Rev. **124**, 1866 (1961).

[47] M. D. Fontana, G. Metrat, J. L. Servoin, and F. Gervais, J. Phys. C **17**, 483 (1984).

[48] M. D. Fontana, G. Dolling, G. E. Kugel, and C. Carabatos, Phys. Rev. B **20**, 3850 (1979).

[49] M. D. Fontana, G. E. Kugel, G. Metrat, and C. Carabatos, Phys. Status Solidi B **103**, 211 (1981).

[50] J. Lascombe, P. V. H. Huong, and S. Kielich, J. Raman Spectrosc. **14**, 219 (1983).

[51] A. M. Quittet, J. L. Servoin, and F. Gervais, J. Phys. (France) **42**, 493 (1981).

[52] D. G. Bozinis and J. P. Hurrell, Phys. Rev. B **13**, 3109 (1976).

[53] A. V. Postnikov, T. Neumann, and G. Borstel, Phys. Rev. B **50**, 758 (1994).

[54] M. D. Fontana, G. E. Kugel, J. Vamvakas, and C. Carabatos, Solid State Commun. **45**, 873 (1983).

[55] L.-M. Li, Y.-J. Jiang, and L.-Z. Zeng, J. Raman Spectrosc. **27**, 503 (1996).

[56] A. D. Bruce, W. Taylor, and A. F. Murray, J. Phys. C **13**, 483 (1980).

[57] K. A. Johnson and N. W. Ashcroft, Phys. Rev. B **58**, 15548 (1998).

[58] J. Heyd, G. E. Scuseria, and M. Ernzerhof, J. Chem. Phys. **118**, 8207 (2003).

[59] J. Heyd, G. E. Scuseria, and M. Ernzerhof, J. Chem. Phys. **124**, 219906 (2006).

[60] S. Cabuk, Optoelectron. Adv. Mater., Rapid Commun. **1**, 100 (2007).

[61] C. M. I. Okoye, J. Phys.: Condens. Matter **15**, 5945 (2003).

[62] E. Wiesendanger, Ferroelectrics **6**, 263 (1974).

[63] F. M. Michel-Calendiri and H. Chermette, J. Phys. C **14**, 1179 (1981).

[64] J. M. Perez-Mato, M. Aroyo, A. García, P. Blaha, K. Schwarz, J. Schweifer, and K. Parlinski, Phys. Rev. B **70**, 214111 (2004).

[65] Y. E. Kitaev, M. I. Aroyo, and J. M. Perez-Mato, Phys. Rev. B **75**, 064110 (2007).